

Ultimate Limits to Optical Displacement Detection in Nanoelectromechanical Systems

T. Kouh*, D. Karabacak*, D. H. Kim** and K. L. Ekinci*

*Aerospace and Mechanical Engineering, Boston University, Boston, MA, USA, tkouh@bu.edu

**On leave from Seoul National University of Technology, Seoul 139-743, Korea, dhkim63@bu.edu

ABSTRACT

We describe an optical technique for the detection of displacement in Nanoelectromechanical Systems (NEMS). The technique is based upon path stabilized optical interferometry. We evaluate the effectiveness of this technique in NEMS by detecting displacements from a series of doubly clamped beam resonators with decreasing dimensions. Our measurements and analyses indicate that the technique tends to become less effective beyond the optical diffraction limit.

Keywords: nanoelectromechanical systems, optical interferometry, displacement detection

1 INTRODUCTION

Nanoelectromechanical Systems (NEMS) are among the most promising manifestations of the emerging field of nanotechnology [1]. These are electromechanical systems with dimensions in the deep submicron — mostly operated in their resonant modes. In this size regime, NEMS come with extremely high resonance frequencies, diminished active masses, tolerable force constants and high quality (Q) factors of resonance. These attributes collectively make NEMS suitable for a multitude of technological applications such as ultra-fast actuators, sensors, and high frequency signal processing components.

There exist fundamental and technological challenges to NEMS optimization. One of the remaining challenges to developing technologies based upon NEMS is a robust, sensitive and broadband displacement detection method for sub-nanometer displacements. Most mainstay displacement sensing techniques used in the domain of Microelectromechanical Systems (MEMS) are not scaleable into the domain of NEMS — necessitating the development of new techniques to realize the full potential of NEMS.

Optical detection, including path stabilized interferometry and Fabry-Perot interferometry, has been used extensively in the domain of MEMS. Using path stabilized interferometry, for instance, shot noise limited displacement sensitivities, $\sqrt{S_x} \sim 10^{-6} \text{ nm}/\sqrt{\text{Hz}}$ are routinely attainable on objects — such as AFM cantilevers — with cross sections much larger than the diffraction limited optical spot [2]. Unfortunately, this conventional approach fails for objects with smaller cross sections [3]. The signal reflected from a NEMS device, for instance, will

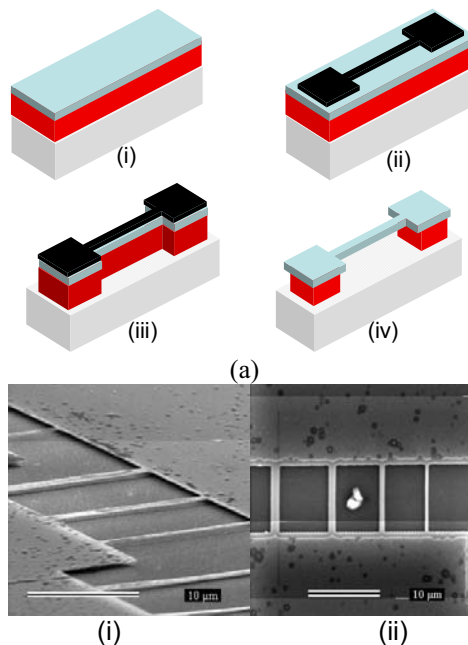


Figure 1: (a) Surface nanomachining of NEMS. A semiconductor heterostructure with structural (top) and sacrificial (middle) layers on top of a substrate (bottom) is patterned using electron beam lithography and selective etch processes. (b) Scanning electron micrographs of silicon doubly-clamped beams.

have a complicated diffraction form — most likely reducing the above-mentioned sensitivity.

In this work, our main objective is to explore the applicability of optical interferometry to NEMS displacement detection — first, by experimentally investigating optical displacement detection in silicon NEMS and then by developing a theoretical picture.

2 EXPERIMENT

Now, we turn to a detailed description of the experimental procedure. We first illustrate the method for fabrication of suspended single crystal silicon structures, and then describe the optical measurements.

The fabrication process is illustrated in Figure 1 (a). The starting material for device fabrication is a silicon-on-insulator (SOI) wafer with a 219 nm-thick silicon device layer on top of 396-nm-thick oxide layer. Fabrication begins by defining large area contact pads by optical lithography. A 40-nm-thick layer of Cr is then evaporated

and, subsequently, standard liftoff is carried out with acetone. Samples are then coated with a bi-layer PMMA (polymethyl methacrylate) resist prior to patterning by electron beam lithography. After resist exposure and development, 40 nm of Cr is evaporated on the samples, followed by liftoff in acetone. The pattern in the Cr metal mask is then transferred to the oxide layer beneath it by anisotropic reactive ion etching (RIE). We use a plasma of CF_4 and O_2 at a pressure of 300 mTorr with respective flow rates of 50 sccm and 5 sccm, and a microwave power of 300 W. The etch rate under these conditions is ~ 6 nm/s. The vertically-etched structures are then released by a controlled selective isotropic etching of the underlying oxide layer using hydrofluoric acid (HF). Figure 1 (b) shows scanning electron micrographs of completed NEMS devices.

The measurements on fabricated devices are carried out inside an ultrahigh vacuum (UHV) chamber using a path stabilized optical interferometer. The block diagram of this set up is displayed in Figure 2 (a). After fabrication, the devices are introduced into the main chamber through a load lock and transferred onto a single-axis linear translator. The motion of the translator brings the devices towards an optical view-port as shown in the Figure 2 (b) — allowing probing of the devices by a laser beam.

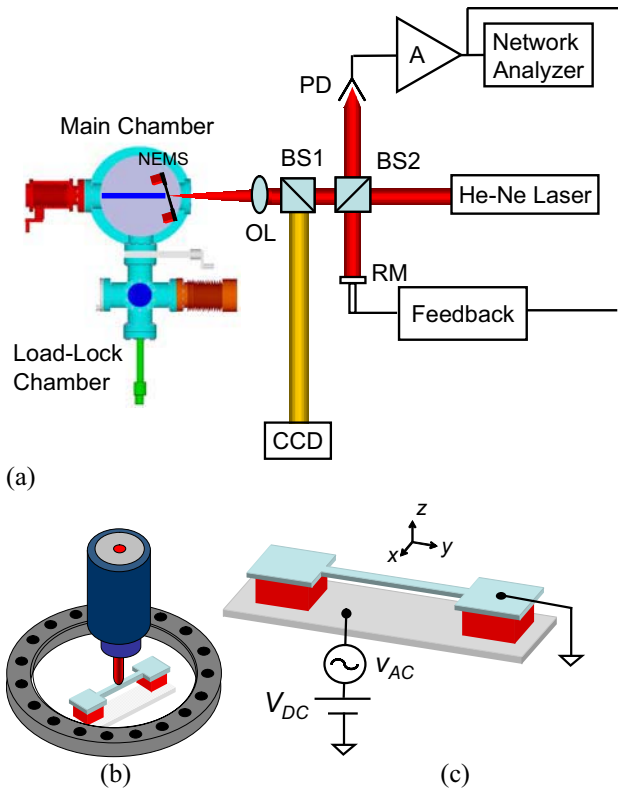


Figure 2: (a) Schematic diagram of the optical measurement setup and the UHV chamber. (b) Close up of the NEMS device in the vicinity of the quartz optical view-port. (c) Schematic diagram of the electrostatic actuation.

The whole optical interferometer is mounted on a XYZ translation stage. The interferometer comprises various beam-splitters (BS), a reference mirror (RM) and a photodetector (PD) as shown in Fig. 2 (a). Coherent light from a He-Ne laser with wavelength, $\lambda \approx 635$ nm is split into two beams — the first beam traveling along a reference path and a second beam used as a probe for NEMS displacement detection. A feedback circuit and a mirror mounted on a piezoelectric actuator control the length of the reference path. The probe beam used for NEMS displacement detection is focused on the device by a 50X objective lens (OL) with numerical aperture, $NA=0.5$. The light reflecting from the NEMS is collected by the same lens.

The probe beam reflected from the NEMS device and the beam in the reference path form an interference pattern on the photodetector. The optical path length that the probe beam travels and consequently, the intensity of the interference pattern on the photodetector change as the NEMS device displaces out of plane (in the z -direction). The intensity variations on the photodetector are measured by a network analyzer.

The NEMS devices are actuated electrostatically [4] and their displacements are detected using a network analyzer as shown in Figure 2 (c). The electrostatic force, F_e , exerted on the doubly clamped beam as a function of the applied voltage, V , can be written as $F_e = -\frac{1}{2} \frac{\epsilon_0 w L}{(d-z)^2} V^2$

where ϵ_0 is the permittivity of free space, d is the initial gap between the beam and the substrate, z is the displacement of the beam, w and L are the width and length of the beam, respectively. In general, the excitation voltage, V includes both V_{DC} and v_{AC} components.

3 RESULTS

We now turn to a discussion of our experimental results. Figure 3 shows the out-of-plane fundamental resonance frequencies of a family of doubly-clamped silicon beams, with rectangular cross sections and different aspect ratios (length/width). The beams are 10 μm long and 200 nm thick with widths of 1000 nm, 750 nm, 500 nm and 250 nm. There is a metallization layer of 1 nm Cr and 1.5 nm Au atop the beams. This particular family of devices yields out-of-plane resonant frequencies between 16.5 MHz and 17.1 MHz. Quality (Q) factors measured were in the range $300 < Q < 3000$ at room temperature.

The fundamental resonance frequency, $\omega_0 / 2\pi$, of a doubly-clamped beam of length, L , and thickness, t , varies linearly with the geometric factor t/L^2 according to the simple relation $\omega_0 / 2\pi = 1.03(\sqrt{E/\rho})t/L^2$ where E is the Young's modulus and ρ is the mass density. The measured frequencies are within 4% of the theoretical predictions.

The inset in Figure 3 shows the rms displacement of the center of the 1000 nm-wide beam as a function of V_{DC}

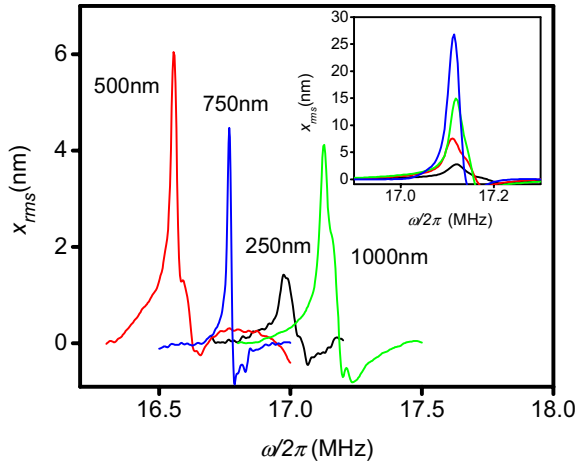


Figure 3: Frequency spectrum of four suspended silicon beams of 10 μm -long (L) and 200 nm-thick (t) with different widths (w) of 1000 nm, 750 nm, 500 nm and 250 nm. The inset shows the frequency spectrum of the silicon beam of 10 $\mu\text{m} \times 200 \text{ nm} \times 1000 \text{ nm}$ as a function of DC driving amplitude, V_{DC} . The lowest curve corresponds to 1 V and V_{DC} is increased by 1V at fixed AC voltage of 800mV. All the measurements are done at 2×10^{-9} Torr.

while v_{AC} is fixed at 800 mV. With increasing V_{DC} , the beam is driven into larger rms amplitude as described above.

4 ANALYSIS

The purpose of the numerical analysis is to gain an understanding of the ultimate limits to optical interferometric displacement detection in NEMS. The measured signal is the photodetector current that flows as a result of the intensity modulations — arising from the NEMS motion — in the interference pattern formed upon the photo-detector.

Obviously, the dimensions of the NEMS beams are on the order of the wavelength of the light used for detection. This necessitates a detailed modeling of the behavior of the electromagnetic (EM) field in the near field region of the NEMS — as many of the analytical solutions based on far-field approximations fail in this size regime.

Our numerical analysis is for a 2-dimensional case. The computation is based on solving Maxwell's Equations for a source free medium with monochromatic light, in the region of focus around the resonator using a finite element method. The laser beam is modeled as an in-plane Gaussian beam of transverse electric (TE) polarization as shown in Figure 4 (a) [5]. The finite element EM field solutions are obtained for the domain, shown in Fig. 4 (a) along the path of the Gaussian beam.

The resonator is modeled to be within the focused region and the surfaces are assumed perfectly reflective.

The center location of the beam is then displaced at various amplitudes to simulate the resonator motion. The displacement of the resonator affects the electric field pattern reflected back to the photodetector. A representative intensity modulation on the photo-detector is shown in Figure 5 (a). Here, the peak intensity is observed to drop significantly as the beam moves between two displacement maxima, x_{max} and $-x_{max}$. The intensity variations thus determined are integrated across the first light fringe for x_{max} and $-x_{max}$ for different rms amplitudes of vibration. Figure 5 (b) shows the weakly parabolic relationship — obtained from multiple simulations — between rms vibration amplitude and the power oscillation observed on the detector.

At temperature, T , the spectral density of the thermomechanical displacement fluctuations of the resonator is given by $S_x = 4k_B T Q / m \omega_o^3$ where k_B is the Boltzmann constant, Q is the quality factor, m is the effective mass of the resonator, and ω_o is the resonant frequency [6]. For our silicon beams of dimensions 10 $\mu\text{m} \times 200 \text{ nm} \times 1000 \text{ nm}$ with $Q \sim 1000$ at room temperature,

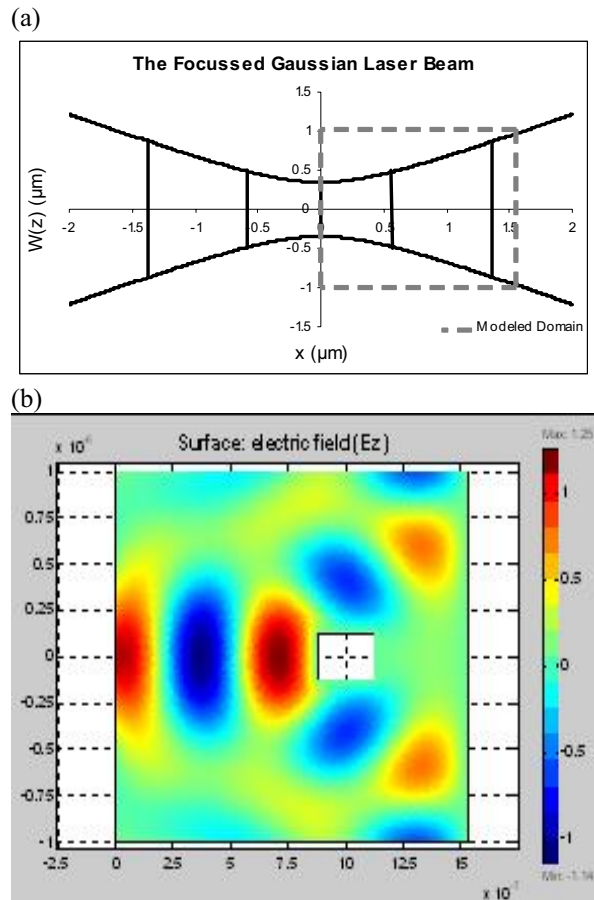


Figure 4: (a) The numerical computation domain modeled in the focus region of the Gaussian laser beam. (b) Electric field in the near-field region of the beam cross section, at stationary position (dimensions in μm).

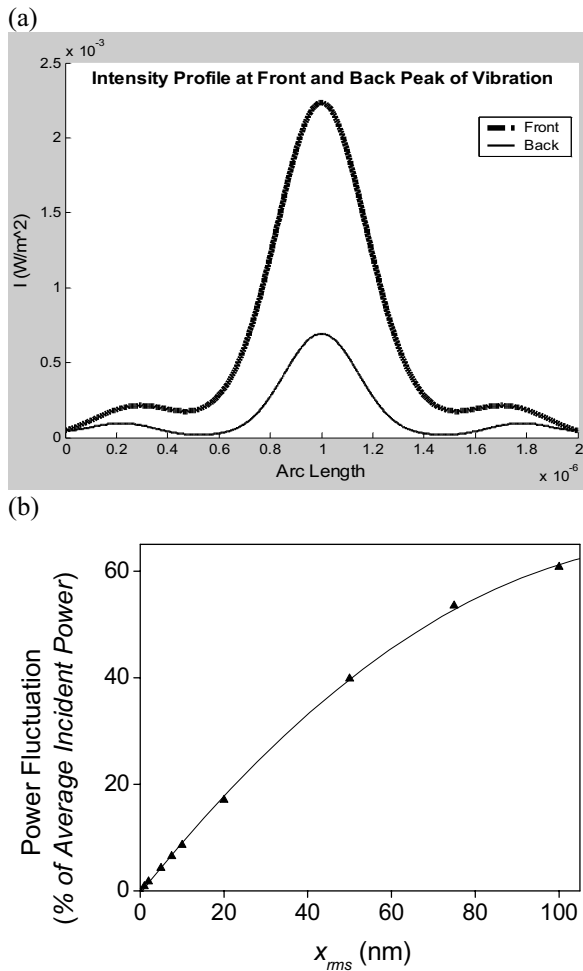


Figure 5: (a) Intensity profile change of interference of the reflected and reference beams, for a vibration range of ± 100 nm. (b) Change in power incident on photodiode based on amplitude of vibration of resonator, for a beam of 250 nm thickness and width.

$\sqrt{S_x} \approx 0.1 \text{ pm} / \sqrt{\text{Hz}}$. We were not able to observe these fluctuations in our optical measurements.

Our displacement sensitivity in this work is determined by the various noise sources in the detection circuit. Figure 6 shows the circuit diagram of the photodetector. The noise sources are shown in lighter shades. The shot noise current spectral density, S_i^{shot} is given by $S_i^{shot} = \eta e^2 P_o / \hbar \omega$ where η is the quantum efficiency of the photodetector, e is the electronic charge, \hbar is the Planck's constant, ω is the frequency of the photon, and P_o is the average power incident on the photodetector [7]. For the typical values of $\eta \sim 10\%$, $\hbar \omega \sim 3 \times 10^{-19} \text{ J}$, and $P_o \sim 10 \mu\text{W}$, $S_i^{shot} \approx 0.1 \text{ pA}^2 / \text{Hz}$. The dark current noise current spectral density, S_i^D is $2eI_D$ where I_D is the dark current. For our photodetector, $I_D \sim 2.5 \text{ nA}$ and the corresponding $S_i^D \approx 10^{-3} \text{ pA}^2 / \text{Hz}$. The amplifier noise in this work is $S_i^a \approx 44 \text{ pA}^2 / \text{Hz}$ [8]. These noise current spectral

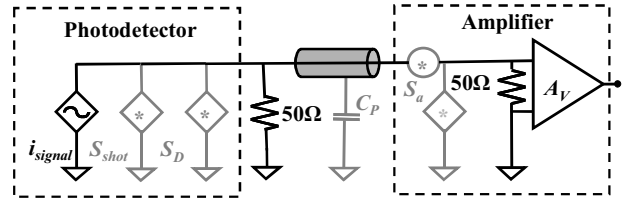


Figure 6: Circuit representation of the detection circuit. The gray elements indicate the noise sources in the circuit such as shot noise, dark current noise, and amplifier noise.

densities determine our sensitivity limits as $S_x = S_i / \left| \partial i_{signal} / \partial x \right|^2$. In our optical path stabilized interferometer, $\partial i_{signal} / \partial x \sim \ln A / \text{nm}$. This gives the total displacement noise spectral density from the photodetector and the amplifier as $S_x^{total} = S_x^{shot} + S_x^D + S_x^a$. This corresponds to the displacement sensitivity of $\sqrt{S_x^{total}} \approx 7 \text{ pm} / \sqrt{\text{Hz}}$.

5 CONCLUSIONS

We have presented experimental and theoretical studies on optical displacement detection in silicon NEMS using a path stabilized interferometer. We measured out of plane fundamental resonance of silicon NEMS with dimensions as small as $10 \mu\text{m} \times 200 \text{ nm} \times 1000 \text{ nm}$ in UHV at room temperature.

The circuit analysis of the optical displacement detection scheme shows that the sensitivity of the path stabilized optical interferometer is limited by the amplifier noise.

We gratefully acknowledge support from the NSF under grants 210752, 216274 and 324416.

REFERENCES

- [1] A. N. Cleland, M. L. Roukes, Applied Physics Letters 69, 2653, 1996.
- [2] T.R. Albrecht, P. Grütter, D. Rugar, D.P.E. Smith, Ultramicroscopy 42, 1638, 1992.
- [3] D. W. Carr and H. G. Craighead, J. Vac. Sci. Technol. B 15, 2760, 1997.
- [4] B. Choi and E. G. Lovell, Journal of Micromechanics and Microengineering, 7, 24, 1997.
- [5] FEMLAB[®] Computation Package, Comsol AB.
- [6] A.N. Cleland, "Foundations of Nanomechanics", Springer, 2003.
- [7] J. W. Wagner, Physical Acoustics 19, 201, 1990.
- [8] FEMTO Messtechnik GmbH, Paul-Lincke-Ufer 34, D-10999 Berlin, Germany.